



## Article

# Numerical Simulation of Impact of Different Redox Couples on Flow Characteristics and Electrochemical Performance of Deep Eutectic Solvent Electrolyte Flow Batteries

Zhiyuan Xiao <sup>1,2,†</sup>, Ruiping Zhang <sup>1,3,†</sup>, Mengyue Lu <sup>1</sup>, Qiang Ma <sup>1</sup> , Zhuo Li <sup>1</sup>, Huaneng Su <sup>1</sup>, Huanhuan Li <sup>4</sup> and Qian Xu <sup>1,\*</sup> 

<sup>1</sup> Institute for Energy Research, Jiangsu University, Zhenjiang 212013, China; zhiyuanx98@vt.edu (Z.X.); 2212106027@stmail.ujs.edu.cn (R.Z.); lumengyue@ujs.edu.cn (M.L.); maqiang@ujs.edu.cn (Q.M.); lizhuo@ujs.edu.cn (Z.L.); suhuaneng@ujs.edu.cn (H.S.)

<sup>2</sup> Department of Mechanical Engineering, Virginia Tech, Blacksburg, VA 24060, USA

<sup>3</sup> China Petroleum & Chemical Corporation Jiangsu Oilfield Branch, Yangzhou 225100, China

<sup>4</sup> Automotive Engineering Research Institute, Jiangsu University, Zhenjiang 212013, China; lihh@ujs.edu.cn

\* Correspondence: xuqian@ujs.edu.cn; Tel.: +86-511-88799500

† These authors contributed equally to this work.

**Abstract:** A comprehensive, three-dimensional, macro-scale model was developed to simulate non-aqueous deep eutectic solvent (DES) electrolyte flow batteries. The model's feasibility was validated by comparing the simulated polarization data with the experimental results. Utilizing this model, the work reported here compared the flow characteristics and electrochemical properties of electrolytes with different redox couples within the porous electrodes of the batteries. Despite variations in the active materials, the distribution of the electrolyte flow rate showed uniformity due to consistent electrode and flow channel designs, indicating that the structural design of electrodes and channels has a more significant impact on electrolyte flow than the physicochemical properties of the electrolytes themselves. This study also highlighted that TEMPO and Quinoxaline DES electrolytes exhibited less flow resistance and more uniform concentration distributions, which helped reduce overpotentials and enhance battery energy efficiency. Furthermore, this research identified that the highest average overpotentials occurred near the membrane for all the redox couples, demonstrating that electrochemical reactions in DES electrolyte flow batteries primarily occur in the region close to the membrane. This finding underscores the importance of optimizing active redox ions transport in electrolytes to enhance electrochemical reactions in the proximal membrane region, which is crucial for improving flow battery performance.

**Keywords:** flow batteries; numerical simulation; redox couples; flow dynamics; electrochemical performance



Academic Editor: Dino Tonti

Received: 11 December 2024

Revised: 26 December 2024

Accepted: 3 January 2025

Published: 7 January 2025

**Citation:** Xiao, Z.; Zhang, R.; Lu, M.; Ma, Q.; Li, Z.; Su, H.; Li, H.; Xu, Q. Numerical Simulation of Impact of Different Redox Couples on Flow Characteristics and Electrochemical Performance of Deep Eutectic Solvent Electrolyte Flow Batteries. *Batteries* **2025**, *11*, 18. <https://doi.org/10.3390/batteries11010018>

**Copyright:** © 2025 by the authors. Licensee MDPI, Basel, Switzerland. This article is an open access article distributed under the terms and conditions of the Creative Commons Attribution (CC BY) license (<https://creativecommons.org/licenses/by/4.0/>).

## 1. Introduction

### 1.1. Research Background and Current Status of Battery Technology Research

Amidst global challenges, like climate change and energy security, China stands out as a significant energy consumer with ambitious initiatives aimed at transitioning to cleaner energy sources. The Chinese government has enacted comprehensive strategies, such as the “Energy Development Strategic Action Plan (2014–2020)” and the “Energy Technology Innovation Plan of Action (2016–2030)”, to expedite the development of renewable resources, enhance energy efficiency, and reduce carbon emissions [1,2]. These policies

underscore China's commitment to sustainable energy production and consumption [3,4]. With renewable energy increasingly incorporated into China's energy portfolio, the role of energy storage technologies has become crucial, especially to counter the intermittency and variability of renewable sources [5,6]. Energy storage systems are pivotal in balancing supply and demand, ensuring the reliability and stability of power transmission.

Flow batteries, with their unique ability to scale as needed and modularity, are garnering attention as a viable solution for extensive energy storage needs. They are less prone to thermal risks and operational hazards due to their design, separating the electrolytes and power stacks, thus enhancing operational safety [7]. Moreover, their ability to undergo several charge–discharge cycles reduces the long-term operational costs and supports environmental sustainability [8]. Given these attributes, flow batteries represent a promising opportunity for future energy storage solutions to support the broad adoption of renewable energy sources, fostering the transition to a more sustainable and secure energy landscape.

The recent advancements in battery technology have been encapsulated in a series of scholarly articles, each contributing distinct insights into the ongoing enhancement of energy storage systems. One study delves into the stability improvements of Vanadium redox flow batteries through innovative electrolyte formulations, promising extended efficiency and durability crucial for modern energy demands [9]. Another explores the development of sodium-ion batteries, highlighting the optimization of cathode materials to make these alternatives more cost-effective and efficient compared to traditional lithium-ion batteries [10]. A further discussion addresses the cost-reduction strategies in battery production, focusing on the longevity and sustainability of electrode materials to bolster commercial viability [11]. Additionally, polymer electrolytes are reviewed for their role in enhancing the safety and operational performance of batteries, underscoring the transformative potential of these materials [12]. Lastly, significant structural innovations in battery architecture are considered for their ability to increase energy density and improve the discharge rates, which are essential for high-demand applications [13]. These studies collectively reflect a robust effort to refine energy storage technologies, ensuring they meet the future sustainability and efficiency standards.

### *1.2. Introduction, Advantages and Disadvantages, and Current Research Status of Deep Eutectic Solvents*

With the growing global demand for renewable energy and efficient energy storage systems, non-aqueous redox flow batteries (NARFBs) have gained significant attention in recent years as an emerging energy storage technology. Compared to the traditional aqueous-based redox flow batteries, NARFBs utilize non-aqueous solvents as the electrolyte medium, demonstrating a broader electrochemical window and higher potential energy density, thus opening new pathways for enhancing the performance of redox flow batteries. The wider electrochemical window of non-aqueous solvents allows for the use of active materials with a higher potential difference in redox flow batteries, thereby increasing the battery's voltage output. Additionally, non-aqueous solvents typically offer good chemical stability and low volatility, which favor the stability and safety of batteries during long-term operation [14–16].

Non-aqueous solvents can generally be divided into three main categories: organic solvents, ionic liquids, and deep eutectic solvents (DESs). Organic solvents pose toxicity and volatility risks, limiting their development. Ionic liquids, while promising, are hindered by high production costs and complex preparation processes. To address these challenges, other researchers have developed deep eutectic solvents (DESs), which feature excellent chemical and thermal stability, enhanced environmental friendliness, and cost-effectiveness. Additionally, DESs are considered outstanding electrolyte solvents due to their excellent

solubility and high ionic conductivity, and their biodegradability and low toxicity align well with the current pursuits of environmentally friendly energy technologies [17–19].

Deep eutectic solvents are mixtures formed through hydrogen bonding interactions between two or more components, with melting points significantly lower than those of the individual components. Due to their unique physicochemical properties, such as a wide electrochemical window, good solvency, low volatility, and relatively low toxicity and cost, these solvents have shown broad application potential across various fields, including, but not limited to, electrochemistry, green chemistry, and bioengineering. DESs can be categorized into four types based on their composition, quaternary ammonium salts + metal salts, quaternary ammonium salts + hydrogen bond donors, metal salts + amino acids, and organic acids + alcohols, with the advantages and disadvantages of each summarized in Table 1.

**Table 1.** Classification of DESs and their advantages and disadvantages.

DES Type	Composition	Advantages	Disadvantages
I	Quaternary Ammonium Salt + Metal Salt	Good conductivity and solubility	Metal salts may increase cost and corrosion risk
II	Quaternary Ammonium Salt + Hydrogen Bond Donor	Wide electrochemical window, good thermal stability, and biodegradability	Lower solubility capacity, potential volatility or toxicity risk
III	Metal Salt + Amino Acid	Good biocompatibility and specific catalytic activity	Narrow electrochemical window, high cost of amino acids
IV	Organic Acid + Alcohol	Good chemical stability, environmentally friendly	High viscosity and low conductivity

### 1.3. Current Status of Modeling DES Electrolyte Flow Battery Research

Regarding the current state of DES flow battery modeling, several types of model have been developed and applied. Continuum models are used to simulate the overall behavior of flow batteries, including fluid dynamics, mass transport, and current distribution. Computational Fluid Dynamic (CFD) models are commonly used to evaluate changes in concentration gradients under different operating conditions and to analyze reactant distribution across electrode surfaces [20]. Porous media models are also used to simulate the transport and reaction processes within the porous structure of the electrodes, which helps to analyze the interactions between electrode materials and DESs, as well as assess performance under various operating conditions [21].

In terms of the redox couples studied in DES-based flow batteries, the Iron–Vanadium (Fe–V) system has been extensively investigated due to its success in aqueous electrolytes, with other researchers exploring its applicability in DESs to increase energy density and long-term stability [22]. Another system that has been studied is the TEMPO–Quinoxaline redox couple, which has high electrochemical activity levels and good reversibility, making it suitable for use with organic-based DESs [23]. Additionally, some studies have focused on other organic redox couples that are compatible with DESs, such as Iron–phenanthroline, with the aim of improving energy density and battery efficiency when used in flow battery systems [24].

These studies and modeling approaches provide strong support for understanding the behavior of DESs in flow batteries, while also helping to identify the benefits and challenges of these novel electrolytes under different operating conditions.

### 1.4. Research Content and Significance of This Study

This study focuses on the development of a comprehensive numerical model of a DES-based RFB. The model is designed to capture the nuances of flow and electrochemical

dynamics within the battery's electrodes and across the membrane. It incorporates realistic assumptions about electrode porosity, electrolyte viscosity, and ion transfer properties, making it a robust tool for predicting battery performance under various operating conditions. The model's predictions are validated against experimental data, ensuring its accuracy and reliability.

The primary aim of the simulation is to elucidate how the choice of redox couples influences the flow characteristics within the electrodes, the distribution of material concentration, the overpotential profiles, and ultimately the overall electrochemical performance of the battery. By systematically analyzing these aspects, this study provides valuable guidance for selecting the optimal redox couple and designing battery systems that offer an improved performance and cost-effectiveness. The insights gained from this research are expected to contribute significantly to the ongoing development of scalable and efficient redox flow batteries, propelling them closer to widespread commercial adoption in energy storage systems.

## 2. Numerical Model

### 2.1. Model Domain and Assumptions

To explore the effects of different redox couples on DES electrolyte flow batteries, a model based on parallel flow channels was developed (as illustrated in Figure 1). The model consists of positive and negative electrodes, flow channels on both sides of these electrodes, and an anion exchange membrane. COMSOL Multiphysics<sup>®</sup> (6.1.0.252), commercial software widely used for solving multiphysics problems, was chosen for this purpose. The software is well suited for addressing the complex physical phenomena within batteries, such as fluid dynamics, electrochemistry, and thermal transfer. COMSOL provides the capability to couple these physical processes accurately, thus enabling realistic simulations of the intricate internal physical phenomena of batteries. The model was created using COMSOL Multiphysics<sup>®</sup> software with the relative tolerance set to  $1.0 \times 10^{-5}$ .

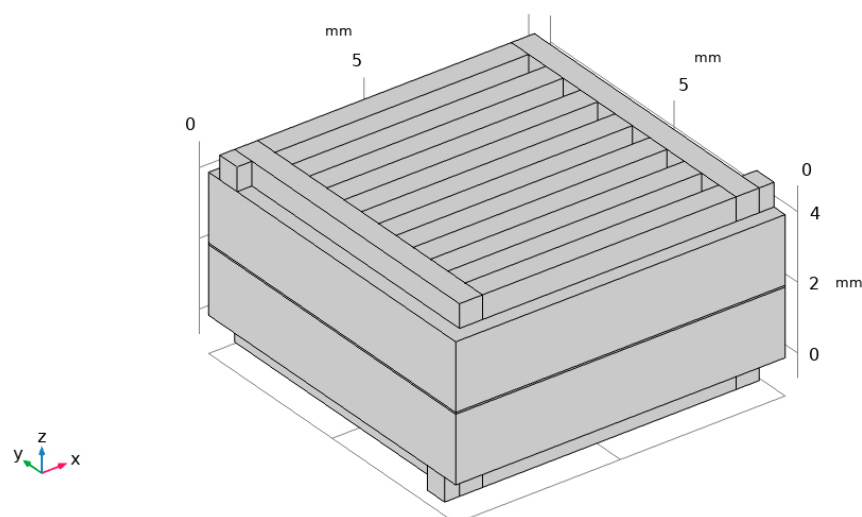


**Figure 1.** Diagram of simplified model.

The simulation of flow batteries involves numerous complex physical processes that are difficult to calculate precisely. Therefore, assumptions are made to simplify the model. These assumptions make the mathematical model solvable and reduce computational costs, while capturing the essential behaviors and characteristics of the system. The model is based on the following assumptions:

(1) The battery operates at a low discharge current density, and the amount of heat generated by chemical reactions within the battery is minimal. Therefore, we ignore the internal reaction heat of the battery and the effects of thermal conduction and convection [25].

(2) It is assumed that only chloride ions can transfer across the membrane, while the other ions do not [26].

(3) The electrolyte is assumed to be incompressible fluid [27].

(4) It is assumed that the electrode, electrolyte, and membrane mass and charge transfer have isotropic properties [28].

(5) The model assumes a steady state for the discharge process, with the discharge current density being a constant value [29].

## 2.2. Control Equations

Darcy's law indicates that the velocity (volumetric flow rate) of fluid passing through a porous medium is directly proportional to the pressure gradient imposed on the medium and inversely proportional to the medium's inherent permeability and the viscosity of the fluid. Flow battery electrodes are commonly made from porous carbon materials with many tiny pores, allowing the electrolyte to pass through. Thus, Darcy's law can be used to describe the flow of electrolyte through the porous electrode material in batteries [30]:

$$\rho \nabla \cdot \mathbf{v} = 0 \quad (1)$$

$$\nabla P + \frac{\mu}{K} \mathbf{v} = 0 \quad (2)$$

where  $\rho$  ( $\text{kg}\cdot\text{m}^{-3}$ )—density of the electrolyte;

$\mathbf{v}$  ( $\text{m}\cdot\text{s}^{-1}$ )—flow velocity of the electrolyte;

$P$  (Pa)—required pressure for electrolyte flow;

$\mu$  (Pa·s)—dynamic viscosity;

$K$  ( $\text{m}^2$ )—permeability of the electrode. This can be calculated using the Carman–Kozeny equation:

$$K = \frac{d_f^2 \varepsilon^3}{K_{CK} (1 - \varepsilon)^2} \quad (3)$$

where  $d_f$  (m)—diameter of carbon fibers;

$\varepsilon$ —porosity of the electrode;

$K_{CK}$ —a model constant related to the choice of porous media material, usually used as a fitting parameter.

The transfer of material through the porous electrode involves liquid-phase mass transfer processes, which typically include diffusion, convection and electromigration. The Nernst–Planck equation, a fundamental equation describing ion migration in electrolytes, incorporates ion diffusion, migration, and convection effects to describe the ion transport process. This equation is crucial for studying and designing electrochemical processes in flow batteries and helps predict ion concentration distribution within a battery's internal electrolyte. Therefore, the Nernst–Planck equation is utilized for these calculations [31]:

$$\nabla \cdot \left( -D_i^{eff} \nabla c_i - Z_i \mu_i^{eff} F c_i \nabla \varphi_l \right) + \mathbf{v} \cdot \nabla c_i = 0 \quad (4)$$

where  $C_i$  ( $\text{mol}\cdot\text{m}^{-3}$ )—concentration of species  $i$ ;

$Z_i$ —charge number of species  $i$ ;

$F$  ( $\text{C}\cdot\text{mol}^{-1}$ )—Faraday constant;

$\varphi_l$  (V)—liquid-phase potential;

$D_i^{eff}$  ( $\text{m}^2 \cdot \text{s}^{-1}$ )—effective diffusion coefficient of species  $i$ , typically adjusted using the Bruggeman correction as shown in Equation (5).

$\mu_i^{eff}$  is effective ion mobility, usually given by the Nernst–Einstein equation

$$D_i^{eff} = \varepsilon^{1.5} D_i \quad (5)$$

$$\mu_i^{eff} = \frac{D_i^{eff}}{RT} \quad (6)$$

where  $R$  ( $\text{J} \cdot \text{mol}^{-1} \cdot \text{K}^{-1}$ )—gas constant;

$T$  (K)—temperature.

The currents in the liquid and solid phases of the electrolyte and the electrode, respectively, can be calculated using principles similar to Ohm's law, as shown in Equations (7) and (8):

$$i_l = -\sigma_l^{eff} \nabla \varphi_l \quad (7)$$

$$i_s = -\sigma_s^{eff} \nabla \varphi_s \quad (8)$$

where  $\sigma_l^{eff}$  ( $\text{S} \cdot \text{m}^{-1}$ )—effective liquid-phase (electrolyte) conductivity;

$\sigma_s^{eff}$  ( $\text{S} \cdot \text{m}^{-1}$ )—the effective solid-phase (electrode) conductivity.

Both are adjusted for liquid- and solid-phase conductivities using the Bruggeman correction:

$$\sigma_l^{eff} = \varepsilon^{1.5} \sigma_l \quad (9)$$

$$\sigma_s^{eff} = (1 - \varepsilon)^{1.5} \sigma_s \quad (10)$$

Based on the law of charge conservation, the ionic current density in the electrolyte can be derived and linked to the electron current density inside the electrode.

$$\nabla i_s = -\nabla i_l = -\sigma_s^{eff} \nabla^2 \varphi_s = -\sigma_l^{eff} \nabla^2 \varphi_l \quad (11)$$

The discharge process of a flow battery depends on the electrochemical reactions of the redox couples occurring at the positive and negative electrodes. Specifically, in the positive electrode region, the active materials in the electrolyte undergo oxidation reactions, while reduction reactions occur at the negative electrode. Due to these electrochemical reactions, electrons flow from the negative to the positive electrode through the external circuit, forming directed movement that generates an electric current. The electrochemical reaction kinetics at the electrodes, which are vital for the discharge process of the redox flow battery, are described by the Butler–Volmer equation, which provides a detailed expression linking the concentrations of reactants, overpotentials, and current densities [32].

$$j_1 = i_1^0 \left[ \frac{c_{Fe(III)}^s}{c_{Fe(III)}} \exp\left(-\frac{\alpha_{1.c} F \eta_1}{RT}\right) - \frac{c_{Fe(II)}^s}{c_{Fe(II)}} \exp\left(-\frac{\alpha_{1.a} F \eta_1}{RT}\right) \right] \quad (12)$$

$$j_2 = i_2^0 \left[ \frac{c_{V(III)}^s}{c_{V(III)}} \exp\left(-\frac{\alpha_{2.c} F \eta_2}{RT}\right) - \frac{c_{V(II)}^s}{c_{V(II)}} \exp\left(-\frac{\alpha_{2.a} F \eta_2}{RT}\right) \right] \quad (13)$$

$$j_1 = i_1^0 \left[ \frac{c_{TEMPO}^s}{c_{TEMPO}} \exp\left(-\frac{\alpha_{1.c} F \eta_1}{RT}\right) - \frac{c_{TEMPO+}^s}{c_{TEMPO+}} \exp\left(-\frac{\alpha_{1.a} F \eta_1}{RT}\right) \right] \quad (14)$$

$$j_2 = i_2^0 \left[ \frac{c_{Quinoxaline}^s}{c_{Quinoxaline}} \exp\left(-\frac{\alpha_{2.c} F \eta_2}{RT}\right) - \frac{c_{Quinoxaline+}^s}{c_{Quinoxaline+}} \exp\left(-\frac{\alpha_{2.a} F \eta_2}{RT}\right) \right] \quad (15)$$

In Equations (12)–(15), subscripts 1 and 2, respectively, represent the positive and negative electrodes.

$j$  ( $\text{A}\cdot\text{m}^{-2}$ )—current density;

$c_i^s$  ( $\text{mol}\cdot\text{m}^{-3}$ )—concentration of species  $i$  at the electrode surface and in the bulk;

$i^0$  ( $\text{A}\cdot\text{m}^{-2}$ )—exchange current density;

$\eta$  (V)—overpotential;

$\alpha$ —charge transfer coefficient, with subscripts c and a denoting the cathode and the anode, respectively. Additionally, the sum of  $\alpha_c$  and  $\alpha_a$  should equal the number of electrons transferred in the electrochemical reaction ( $n = 1$ ).

During electrochemical processes, when the cathode and anode reactions reach a dynamic equilibrium where the number of electrons produced matches those consumed, the net current within the system is essentially zero. This scenario occurs at each electrode, where the production or consumption of electrons is equal, representing a state with no external current flow, referred to as the exchange current density. The exchange current densities at the anode and cathode  $i_1^0$  ( $\text{A}\cdot\text{m}^{-2}$ ) and  $i_2^0$  ( $\text{A}\cdot\text{m}^{-2}$ ) can be calculated using the following equations.

$$i_1^0 = F \cdot k_1 \cdot (c_{Fe(II)})^{\alpha_{1,c}} \cdot (c_{Fe(III)})^{\alpha_{1,a}} \quad (16)$$

$$i_2^0 = F \cdot k_2 \cdot (c_{V(II)})^{\alpha_{2,c}} \cdot (c_{V(III)})^{\alpha_{2,a}} \quad (17)$$

where  $k$  ( $\text{m}\cdot\text{s}^{-1}$ )—reaction rate constant.

The volume current densities at the anode and cathode  $i_v$  ( $\text{A}\cdot\text{m}^{-3}$ ) can then be expressed as

$$i_{v,1} = a_1 j_1 = a_1 i_1^0 \left[ \frac{c_{Fe(III)}^s}{c_{Fe(III)}} \exp\left(-\frac{\alpha_{1,c} F \eta_1}{RT}\right) - \frac{c_{Fe(II)}^s}{c_{Fe(II)}} \exp\left(-\frac{\alpha_{1,a} F \eta_1}{RT}\right) \right] \quad (18)$$

$$i_{v,2} = a_2 j_2 = a_2 i_2^0 \left[ \frac{c_{V(III)}^s}{c_{V(III)}} \exp\left(-\frac{\alpha_{2,c} F \eta_2}{RT}\right) - \frac{c_{V(II)}^s}{c_{V(II)}} \exp\left(-\frac{\alpha_{2,a} F \eta_2}{RT}\right) \right] \quad (19)$$

where  $a$  ( $\text{m}^{-1}$ )—electrochemical active surface area of the electrode.

The overpotential in the flow battery, which signifies the difference between the actual electrode potential and its equilibrium potential (i.e., the potential without any current flow), represents the extra energy required to drive the electrochemical reactions. The overpotentials at the anode and cathode can be computed using the following equations.

$$\eta_1 = \varphi_{s,1} - \varphi_{l,1} - E_{eq,1} \quad (20)$$

$$\eta_2 = \varphi_{s,2} - \varphi_{l,2} - E_{eq,2} \quad (21)$$

where  $E_{eq}$  (V), is the equilibrium potential, which can be derived from the Nernst equation [33].

$$E_{eq,1} = E_1^0 + \frac{RT}{nF} \ln\left(\frac{c_{Fe(III)}}{c_{Fe(II)}}\right) \quad (22)$$

$$E_{eq,2} = E_2^0 + \frac{RT}{nF} \ln\left(\frac{c_{V(III)}}{c_{V(II)}}\right) \quad (23)$$

where  $E^0$  (V)—standard electrode potential.

This model adopts the boundary conditions of negative grounding. The output voltage can be computed by integrating the solid-phase potential at the positive electrode [34].

$$V_{\text{cell}} = \frac{\int \varphi_{s,1} dS}{S} \quad (24)$$

where  $S$  ( $\text{m}^2$ )—contact area between the electrode and the collector.

Flow batteries rely on the circulation of electrolytes to transport charge carriers between the two half-cells (anode and cathode). This circulation is achieved by pumps that transport the electrolyte from a storage tank to the reaction areas of the battery, and then back to the tank. Although this flow process is crucial for the efficient operation of the flow battery, it also introduces additional energy losses, namely the power loss due to the pump operation,  $P_{\text{pump}}$  (W), which is related to the pump efficiency and the pressure drop and can be calculated using Equation (25).

Moreover, under real discharge conditions, due to polarization effects, the actual output voltage may not reach the ideal voltage, leading to polarization power losses,  $P_{\text{power}}$  (W), which can be expressed by Equation (26).

Adding the power losses due to the pump operation and the losses caused by polarization gives the total power loss during discharge,  $P_{\text{total}}$  (W) calculated using Equation (27).

$$P_{\text{pump}} = \frac{\Delta p_{\text{total}} \cdot Q}{\eta_p} \quad (25)$$

$$P_{\text{power}} = (V_{\text{ideal}} - V_{\text{cell}}) \cdot I \cdot S \quad (26)$$

$$P_{\text{total}} = P_{\text{pump}} + P_{\text{power}} \quad (27)$$

where  $\Delta p_{\text{total}}$  (Pa)—total pressure drop across the anode and cathode;

$Q$  ( $\text{m}^3 \cdot \text{s}^{-1}$ )—inlet flow rate;

$\eta_p$ —pump efficiency;

$V_{\text{ideal}}$  (V)—ideal output voltage, calculated as the absolute difference between the standard electrode potentials of the anode and cathode.  $V_{\text{cell}}$  is obtainable from Equation (24);

$I$ —absolute value of the discharge current density applied on the anode side.

### 2.3. Model Parameters

The model involves various parameters associated with mass transport and electrochemical reaction kinetics. These parameters are summarized in Table 2.

**Table 2.** Parameters applied in simulation.

Symbol	Parameter	Value	Unit	Source
$T$	Temperature	298	K	
$D_{\text{TEMPO}}$	Diffusion coefficient of TEMPO	$2.85 \times 10^{-7}$	$\text{cm}^2 \cdot \text{s}^{-1}$	[35]
$D_{\text{Quinoxaline}}$	Diffusion coefficient of Quinoxaline	$1.26 \times 10^{-5}$	$\text{cm}^2 \cdot \text{s}^{-1}$	[35]
$D_{\text{V(II)}}$	Diffusion coefficient of $\text{V}^{2+}$	$1.16 \times 10^{-9}$	$\text{cm}^2 \cdot \text{s}^{-1}$	[35]
$D_{\text{V(III)}}$	Diffusion coefficient of $\text{V}^{3+}$	$1.16 \times 10^{-9}$	$\text{cm}^2 \cdot \text{s}^{-1}$	[35]
$D_{\text{Cl}}$	Diffusion coefficient of $\text{Cl}^{-1}$	$1.55 \times 10^{-8}$	$\text{cm}^2 \cdot \text{s}^{-1}$	[36]
$D_{\text{Fe(II)}}$	Diffusion coefficient of $\text{Fe}^{2+}$	$1.83 \times 10^{-9}$	$\text{cm}^2 \cdot \text{s}^{-1}$	[35]
$D_{\text{Fe(III)}}$	Diffusion coefficient of $\text{Fe}^{3+}$	$1.83 \times 10^{-9}$	$\text{cm}^2 \cdot \text{s}^{-1}$	[35]
$\alpha_{\text{TEMPO}}$	Transfer coefficient of TEMPO in DES electrolyte	0.482	–	[37]
$k_{\text{TEMPO}}$	Standard reaction rate constant of TEMPO in DES electrolyte	$1.03 \times 10^{-7}$	$\text{cm} \cdot \text{s}^{-1}$	Equation (28)
$\sigma_{\text{TEMPO}}$	Conductivity of TEMPO in DES electrolyte	7.23	$\text{mS} \cdot \text{cm}^{-1}$	[35]



Table 2. Cont.

Symbol	Parameter	Value	Unit	Source
$\mu_{\text{TEMPO}}$	Viscosity of TEMPO in DES electrolyte	30.2	mPa·s	[35]
$\alpha_{\text{Quinoxaline}}$	Transfer coefficient of Quinoxaline in DES electrolyte	0.436	–	[37]
$k_{\text{Quinoxaline}}$	Standard reaction rate constant of Quinoxaline in DES electrolyte	$6.28 \times 10^{-6}$	cm·s <sup>-1</sup>	Equation (28)
$\sigma_{\text{Quinoxaline}}$	Conductivity of Quinoxaline in DES electrolyte	7.49	mS·cm <sup>-1</sup>	[35]
$\mu_{\text{Quinoxaline}}$	Viscosity of Quinoxaline in DES electrolyte	41.7	mPa·s	[35]
$\alpha_{\text{Fe}}$	Transfer coefficient of Iron in DES electrolyte	0.419	–	[37]
$k_{\text{Fe}}$	Standard reaction rate constant of Iron in DES electrolyte	$6.35 \times 10^{-6}$	cm·s <sup>-1</sup>	Equation (28)
$\sigma_{\text{Fe}}$	Conductivity of Iron in DES electrolyte	2.2	mS·cm <sup>-1</sup>	[35]
$\mu_{\text{Fe}}$	Viscosity of Iron in DES electrolyte	43.2	mPa·s	[35]
$\alpha_{\text{V}}$	Transfer coefficient of Vanadium in DES electrolyte	0.445	–	[37]
$k_{\text{V}}$	Standard reaction rate constant of Vanadium in DES electrolyte	$1.02 \times 10^{-5}$	cm·s <sup>-1</sup>	Equation (28)
$\sigma_{\text{V}}$	Conductivity of Vanadium in DES electrolyte	1.332	mS·cm <sup>-1</sup>	[35]
$\mu_{\text{V}}$	Viscosity of Vanadium in DES electrolyte	45.4	mPa·s	[35]
$\sigma_{\text{m}}$	Conductivity of the membrane	0.3	S·m <sup>-1</sup>	[36]
$\varepsilon$	Porosity	0.94	–	[36]
$a$	Specific surface area	35,000	m <sup>-1</sup>	[36]
$\sigma_{\text{e}}$	Electronic conductivity	220	S·m <sup>-1</sup>	[36]
$d_{\text{f}}$	Diameter of carbon fibers	$1.76 \times 10^{-5}$	m	[36]
$L_{\text{e}}$	Length of electrode	0.004	m	[36]
$W_{\text{e}}$	Width of electrode	0.01	m	[36]
$H_{\text{e}}$	Height of electrode	0.01	m	[36]
$L_{\text{channel}}$	Length of flow channel	0.002	m	[36]
$W_{\text{channel}}$	Width of flow channel	0.01	m	[36]
$H_{\text{channel}}$	Height of flow channel	0.002	m	[36]
$L_{\text{m}}$	Thickness of membrane	0.12	mm	[36]
$E_{0\_Quinoxaline}$	Reference equilibrium potential of Quinoxaline	–0.9	V	[38]
$E_{0\_TEMPO}$	Reference equilibrium potential of TEMPO	0.9	V	[39]
$E_{0\_V}$	Reference equilibrium potential of Vanadium	–0.26	V	[36]
$E_{0\_Fe}$	Reference equilibrium potential of Iron	0.769	V	[36]
$C_{0\_neg}$	Initial concentration at the negative electrode	0.1	mol·L <sup>-1</sup>	[36]
$C_{0\_pos}$	Initial concentration at the positive electrode	0.1	mol·L <sup>-1</sup>	[36]
$Q$	Volumetric flow rate	20	ml·min <sup>-1</sup>	[36]
$\rho_{\text{pos}}$	Density of positive electrode electrolyte	1242.74	kg·m <sup>-3</sup>	[36]
$\rho_{\text{neg}}$	Density of negative electrode electrolyte	1246.74	kg·m <sup>-3</sup>	[36]
$K_{\text{CK}}$	CK constant	5.55	–	[36]

The equation used to obtain reaction constant  $k$  is as follows [40,41]:

$$E_P = E_0 - \left[ 0.78 - \ln k + \ln \left( \frac{D\alpha n F v}{RT} \right)^{1/2} \right] \quad (28)$$

where  $E_P$ —potential at which a specific peak occurs during an electrochemical reaction;

$E_0$ —standard electrode potential;

$k$ —reaction rate constant;

$\alpha$ —charge transfer coefficient;

$n$ —number of electrons transferred during the electrochemical reaction;

$F$ —Faraday's constant;

$v$ —scan rate.

This equation relates the observed peak potential ( $E_P$ ) to the intrinsic properties of the electrochemical system, including the thermodynamic parameters ( $E_0$ ), the kinetic parameters ( $k$ ), and the transport properties ( $D$ ). The term involving the logarithms and the square root suggests the presence of mixed control—both kinetic and mass transport

limitations—during the electrochemical process. The peak potential depends on both the rate of electron transfer and the rate of mass transport, particularly when a reaction occurs at high scan rates or for slow diffusion species.

#### 2.4. Boundary Conditions

To ensure the solvability of the problem, effectively reduce the computational domain and volume, and thus enhance the efficiency of the simulation, certain boundary conditions were set. All the boundary conditions applied to the model are summarized in Table 3.

**Table 3.** Boundary conditions applied in model.

Boundary Description	Boundary Condition
Applied current density at the anode	$-\sigma_s^{eff} \nabla \varphi_s \cdot \mathbf{n} = -I$
Grounding at the cathode	$\varphi_s = 0$
Insulation on remaining boundaries	$-\mathbf{n} \cdot \mathbf{i}_l = 0, -\mathbf{n} \cdot \mathbf{i}_s = 0$
Velocity boundary set at the inlet	$v_{in} = Q \cdot (\varepsilon \cdot A)^{-1}$
Pressure boundary set at the outlet	$P_{out} = 0$
No-slip boundary condition on remaining surfaces	$\nabla p \cdot \mathbf{n} = 0$
Concentration boundary set at the inlet	$c_{V(II)_{in}} = c_{0\_neg} \cdot SOC$
	$c_{V(III)_{in}} = c_{0\_neg} \cdot (1 - SOC)$
	$c_{Fe(II)_{in}} = c_{0\_pos} \cdot (1 - SOC)$
	$c_{Fe(III)_{in}} = c_{0\_pos} \cdot SOC$
	$c_{CL\_neg} = 2c_{0\_neg} \cdot SOC + 3c_{0\_neg} \cdot (1 - SOC)$
	$c_{CL\_pos} = 2c_{0\_pos} \cdot (1 - SOC) + 3c_{0\_pos} \cdot SOC$
Zero diffusion flux at the outlet	$c_{TEMPO} = c_0 \cdot SOC$
	$c_{Quinoxaline} = c_0 \cdot (1 - SOC)$
	$-D_i^{eff} \nabla c_i \cdot \mathbf{n} = 0$
Zero flux condition on remaining boundaries	$(-D_i^{eff} \nabla c_i - Z_i \mu_i^{eff} F c_i \nabla \varphi_l + c_i \mathbf{v}) \cdot \mathbf{n} = 0$

#### 2.5. Model Reliability Verification

##### (1) Experimental Materials and Test Equipment

The materials and instruments used in the experiment are shown in Tables 4 and 5, respectively.

**Table 4.** Details of experiment materials.

Material	Specification	Manufacturer
Choline Chloride	Analytical Grade	Macklin Reagent Company, Shanghai, China
Ethylene Glycol	Analytical Grade	Sinopharm Group, Beijing, China
Anhydrous Ethanol	Analytical Grade	Sinopharm Group, Beijing, China
Deionized Water	Grade 1	Ristech Water Purification Technology Co., Ltd., Xiamen, China
N <sub>2</sub>	>99%	Zhenjiang Zhongpu Special Gas Co., Ltd., Zhenjiang, China
VCl <sub>3</sub>	>97%	Aladdin Reagent Company, Shanghai, China
FeCl <sub>2</sub> ·4H <sub>2</sub> O	Analytical Grade	Aladdin Reagent Company, Shanghai, China
Tetramethylpiperidine Oxide (TEMPO)	98%	Aladdin Reagent Company, Shanghai, China
Quinoxaline	>99.0%	Aladdin Reagent Company, Shanghai, China
Graphite Felt	GFA 6 EA, 6 mm	SGL Carbon Company, Shanghai, China
Carbon Paper	TGF-H-090, 0.19 mm	Toray Industries, Shanghai, China
Nafion Membrane	Nafion 212	DuPont, Shanghai, China

**Table 5.** Details of experiment equipment.

Instrument	Model	Manufacturer
Peristaltic Pump	BT100-1F	Lange Constant Flow Pump Co., Ltd., Baoding, China
Glassy Carbon Electrode	GC150	Tianjin Aida, Tianjin, China
Platinum Electrode	213-01	Shanghai INESA Scientific Instrument Co., Ltd., Shanghai, China
Saturated Calomel Electrode	232-01	Shanghai INESA Scientific Instrument Co., Ltd., Shanghai, China
Electronic Balance	FA1004	Shanghai Shangping Instrument Co., Ltd., Shanghai, China
Conductivity Meter	DDS-307A	Shanghai Zhiguang Instrument Co., Ltd., Shanghai, China
Digital Viscometer	LDV-2 + PRO	Shanghai Nirun Intelligent Technology Co., Ltd., Shanghai, China
Heating Magnetic Stirrer	79-1	Shanghai Meixiang Instrument Co., Ltd., Shanghai, China
Battery Testing System	Arbin BT 2000	Arbin Instruments, Beijing, China
Electrochemical Workstation	CHI760E	Shanghai Chenhua Instrument Co., Ltd., Shanghai, China

## (2) Polarization Test (I–V)

Electrochemical performance tests, including polarization tests, were conducted on the electrodes. To learn about the testing methods, refer to the article published by Zhao et al. [42], and the specific test setup parameters are shown in Table 6.

**Table 6.** Electrochemical test parameters.

Name	Parameter	Unit
Positive Electrode Frequency Range	0.01–10 <sup>5</sup>	Hz
Negative Electrode Frequency Range	0.01–10 <sup>6</sup>	Hz
AC Disturbance Voltage	5	mV
Electrolyte Flow Rate	20	mL·min <sup>−1</sup>
Electrode Area	1	cm <sup>2</sup>
Electrode Thickness	3	mm
Charge/Discharge Current Density	2	mA·cm <sup>−2</sup>
Charge/Discharge Cycle Period	20	min
SOC	50	%
Ion Exchange Membrane	Nafion 212	

The polarization test of a flow battery is a crucial electrochemical performance evaluation method designed to analyze and optimize the performance of the battery's electrodes and electrolyte. This test assesses the battery's internal resistance, electrode kinetics, and ion transport characteristics by measuring the variation in battery voltage under different current densities. During the polarization test of a flow battery, the voltage across the battery terminals is closely monitored, while systematically adjusting the current passing through the battery. This is typically achieved by gradually increasing the current load through an external circuit. As the current increases, the electrochemical reactions occurring in the battery electrodes intensify, leading to more significant potential losses, including activation polarization (related to electrode reaction kinetics), ohmic polarization (related to internal resistance), and concentration polarization (related to ion transport in the electrolyte).

The polarization curve is the key result obtained from this test, visually representing the battery's performance. The battery's polarization curve is divided into three distinct regions, the activation polarization region, the ohmic polarization region, and the concentration polarization region, each corresponding to different limiting factors during battery operation. The activation polarization region appears at the initial section of the curve, where the current density is low, and the reaction rate is limited by the activation energy at the electrode surface, reflecting the electrode reaction kinetics. Voltage loss in this region is primarily governed by the charge transfer process on the electrode and increases with the current density. The curve's steep slope in this region indicates that a small increase in current leads to a significant change in potential, thus limiting the battery's performance.

As the current density further increases, the battery enters the ohmic polarization region, where the voltage linearly increases with the current, reflecting the battery system's internal resistance. In this region, the ionic conductivity of the electrolyte and the conductivity of the electrodes and current collectors become the main performance bottlenecks. Finally, at high current densities, the battery reaches the concentration polarization region. In this region, the ion transport rate in the electrolyte cannot meet the high reaction rate demand at the electrode surface, leading to a significant ion concentration drop near the electrodes and the formation of a concentration gradient. Consequently, voltage loss starts to increase sharply, and the curve exhibits a steep decline, indicating the mass transport process's limit. By comprehensively analyzing the polarization curve of the flow battery, it is possible to quantitatively understand the battery's performance in practical operation and identify the main factors affecting its efficiency.

### (3) Polarization Curves Verification

Figure 2 shows the polarization curves of the four battery groups: Fe/V and TEMPO/V (a); and Fe/V and Fe/Quinoxaline (b). The voltages of the TEMPO/V and Fe/Quinoxaline groups are significantly higher than those of the Fe/V group, indicating that the total of activation polarization, ohmic polarization, and concentration polarization is minimized, reducing internal polarization and achieving less voltage loss.

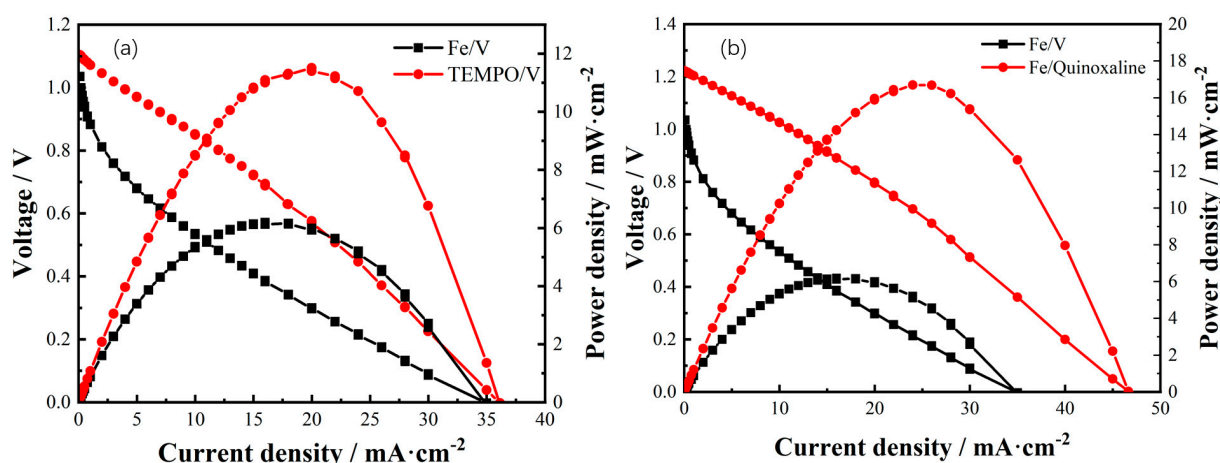


**Figure 2.** Polarization curves of Fe/V and TEMPO/V batteries (a), as well as Fe/V and Fe/Quinoxaline batteries (b).

To further investigate the applicability of the active materials TEMPO/Quinoxaline in the DESs, polarization tests were conducted with three selected concentrations for TEMPO (0.1 M, 0.15 M, and 0.3 M) and three for Quinoxaline (0.05 M, 0.1 M, and 0.15 M). Figure 3 presents the polarization curves of TEMPO/V and Fe/Quinoxaline batteries at different concentrations. The test results indicate that the optimal concentrations are 0.15 M and 0.1 M, respectively.

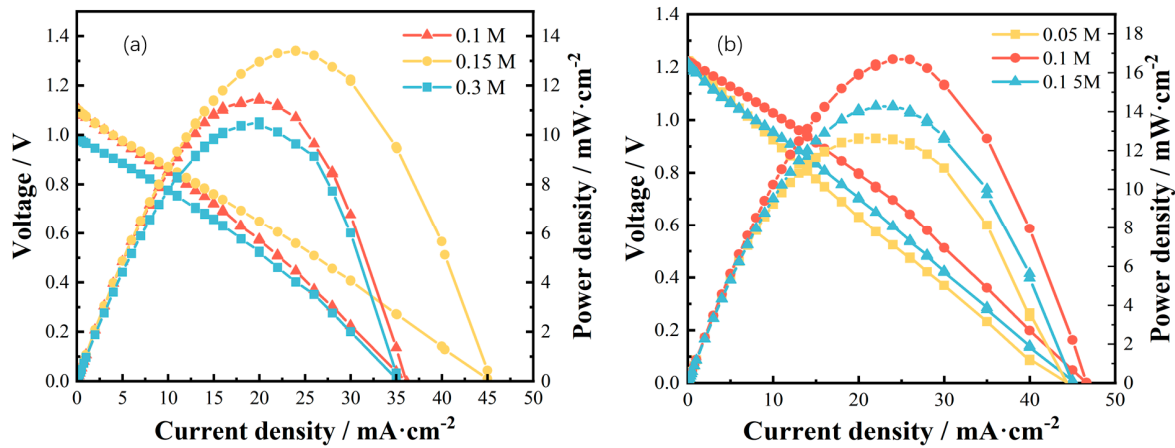


Figure 3. Polarization curves of TEMPO/V (a) and Fe/Quinoxaline (b) batteries at different concentrations.

Polarization tests were conducted on the TEMPO/Quinoxaline single cells under two conditions: the optimal concentration of TEMPO in the DESs (0.15 M) and the optimal concentration of Quinoxaline (0.1 M). The results are shown in Figure 4. Under the condition of a 0.1 M concentration, the cell achieved a peak power density of  $23.38 \text{ mW}\cdot\text{cm}^{-2}$  and a maximum current density of  $55.73 \text{ mA}\cdot\text{cm}^{-2}$ . Under the condition of a 0.15 M concentration, the peak power density and maximum current density were  $22.95 \text{ mW}\cdot\text{cm}^{-2}$  and  $53.99 \text{ mA}\cdot\text{cm}^{-2}$ , respectively. Comparatively, at a concentration of 0.1 M, both the peak power density and maximum current density were slightly higher. Compared with the Fe/V battery, the peak power density and maximum current density of the TEMPO/Quinoxaline battery at 0.1 M concentration increased by 277.50% and 59.32%, respectively. The higher peak power density indicates that the TEMPO/Quinoxaline battery has a greater power output capacity per unit time.

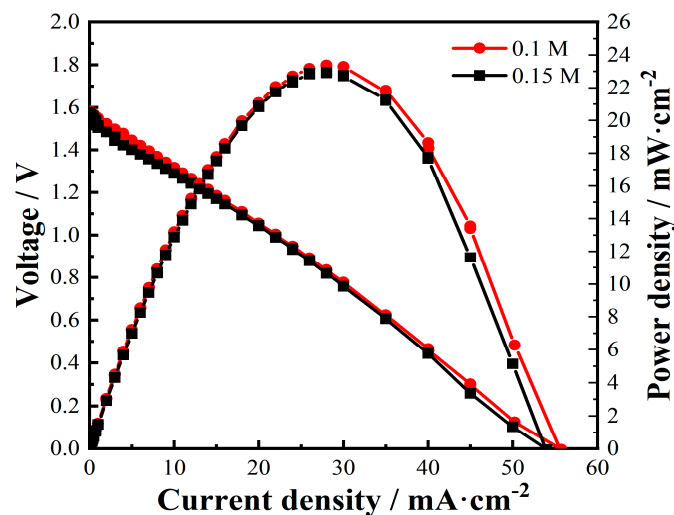
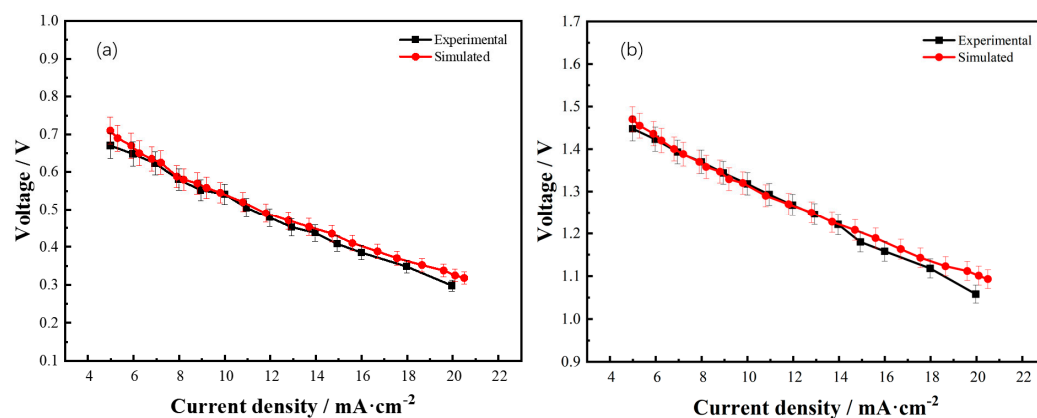


Figure 4. Polarization curves for TEMPO/Quinoxaline battery.

Numerical simulations were conducted for both the Fe/V DES electrolyte flow battery and the TEMPO–Quinoxaline DES electrolyte flow battery, with the results shown in Figure 5. The experimental polarization curves for the Fe/V DES and TEMPO–Quinoxaline DES electrolyte flow batteries were compared with the simulation results. The maximum relative errors for the two battery sets were 4.63% and 4.81%, respectively. These results demonstrate that the experimental data and the simulation data are very similar, indicating that the established model and the set parameters can largely simulate the actual behavior of the batteries under experimental conditions. This indicates that the model has good

reliability in predicting the electrochemical behavior of DES electrolyte flow batteries. Moreover, within the current density range of 6–15 mA·cm<sup>-2</sup>, the simulation results almost completely match the experimental outcomes. Thus, the current density of 10 mA·cm<sup>-2</sup> within this range was selected for subsequent simulations.



**Figure 5.** Polarization curves. (a) Fe–Vanadium DES flow battery, and (b) TEMPO–Quinoxaline DES flow battery.

#### (4) Mesh Independence Verification

To select an appropriate number of grid cells, the output voltage and voltage drop for the Fe/V DES electrolyte flow battery and the TEMPO–Quinoxaline DES electrolyte flow battery were calculated at different grid densities, with the results shown in Figure 6. Figure 6a illustrates how the output voltage changes with an increase in the number of grid cells. It can be observed that as the number of grid cells increases, the output voltage gradually decreases, and then tends to stabilize after reaching 111,000 grid cells. Figure 6b shows how the voltage drop changes with an increase in the number of grid cells. Initially, the voltage drop rises rapidly, and then stabilizes around 111,000 grid cells, eventually settling at about 252,000 Pa. These results indicate that once the number of grid cells exceeds 111,000, the dependency of the output voltage and voltage drop on grid density becomes negligible, showing grid independence. Therefore, after weighing the trade-offs between time and computational resource expenditure, a grid size of 111,000 was chosen for the simulation of DES-based flow batteries.

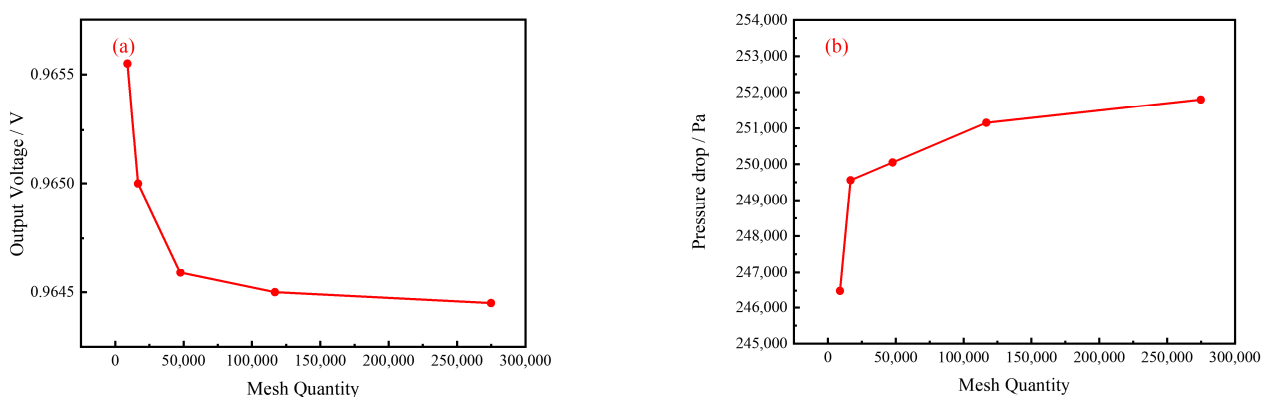


**Figure 6.** Variation in output voltage (a) and voltage drop (b) with mesh quantity.

### 3. Results and Discussion

In this section, the established numerical model is used to explore the impact of different active materials in DES electrolytes on the performance of flow batteries. All the

simulations were carried out under the same conditions for temperature (298 K), discharge current density ( $10 \text{ mA} \cdot \text{cm}^{-2}$ ), and the inlet flow rate ( $0.1 \text{ mL} \cdot \text{min}^{-1}$ ).

### 3.1. Flow Characteristics of Different Redox Couples Electrolytes

The key parameter in the study of flow battery performance is the flow velocity distribution of electrolytes within the electrodes. Uniform flow velocity distribution can significantly enhance the efficiency of the mass transfer processes, ensuring a stable supply of reactants on the electrode surfaces, and thereby ensuring stable electrochemical reactions. To further understand the material transport characteristics of different redox couple electrolytes in flow batteries, this study analyzed the flow velocity distributions of  $\text{FeCl}_2$ , TEMPO,  $\text{VCl}_3$ , and Quinoxaline DES electrolytes within the porous electrodes under consistent inlet flow rates and porosity distributions. The results are shown in Figure 7a–d. The three-dimensional velocity distribution cloud diagrams indicate that despite the flow dynamics of the positive electrolytes ( $\text{FeCl}_2$  and TEMPO) and the negative electrolytes ( $\text{VCl}_3$  and Quinoxaline) being uneven, there is no significant change between them. The consistent flow velocity distribution across different electrolytes can be attributed to the uniformity in electrode and flow channel design. In flow batteries, the design of the flow channel structure significantly impacts the hydrodynamic behavior and resulting electrolyte flow velocity distribution. Specific geometric configurations of flow channels guide the fluid dynamics in a particular manner. Even minor variations in the viscosity or density of the electrolytes do not significantly alter the flow patterns, indicating that the internal structure of the battery has a greater influence on flow velocity distribution than the physical properties of the electrolytes. Also, the Reynold numbers of the electrolyte flows remain similar, indicating similar flow regimes, which is another reason why the flow velocity distribution diagrams do not show significant differences.

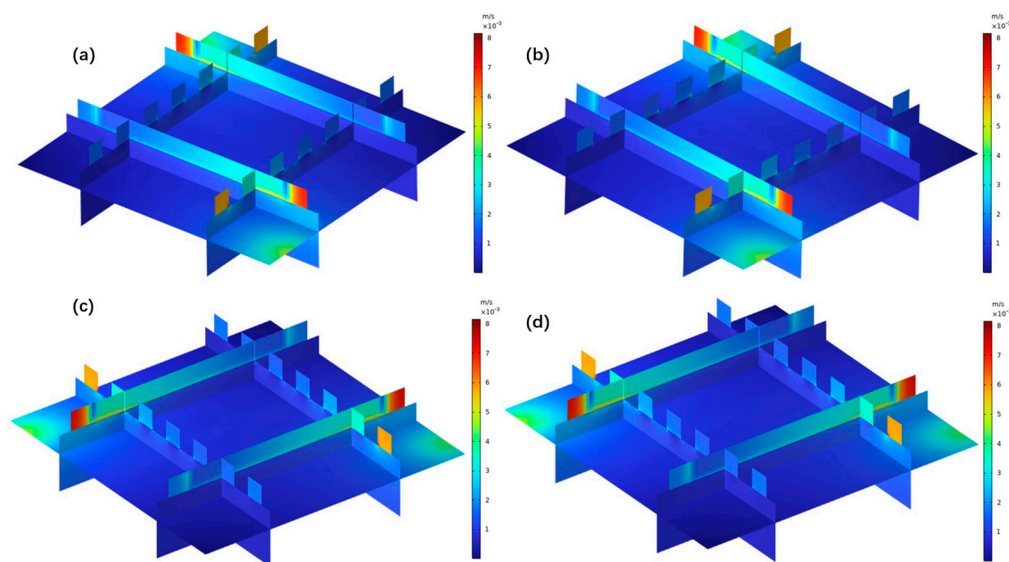


**Figure 7.** Cloud diagram of flow rate distribution of different electrolytes in electrodes. (a)  $\text{FeCl}_2$ , (b) TEMPO, (c)  $\text{VCl}_3$ , (d) and Quinoxaline.

The spatial distribution of pressure drops reflects the flow resistance of the electrolytes within the electrodes. Figure 8 shows the pressure drop distribution of the  $\text{FeCl}_2$ , TEMPO,  $\text{VCl}_3$ , and Quinoxaline DES electrolytes within the porous electrodes. From the three-dimensional cloud diagram, it can be observed that for the two positive electrode electrolytes ( $\text{FeCl}_2$  and TEMPO) and the two negative electrode electrolytes ( $\text{VCl}_3$  and Quinoxaline), the pressure drop of each electrolyte exhibits a pattern of higher inlet pressure and lower outlet pressure. The inlet pressure of the  $\text{FeCl}_2$  DES electrolyte is 1.5 times

that of TEMPO, while the inlet pressure of the  $\text{VCl}_3$  DES electrolyte is 1.15 times larger than that of Quinoxaline. The larger the pressure difference between the entrance and exit of the porous electrodes is, the greater the pressure drop is, which can lead to increased pump power loss during the operation of the flow battery and reduction in battery's energy efficiency. Furthermore, the pressure drops at different locations were also investigated, as shown in Figure 9. The pressure drops at the membrane side, the center of the electrodes and the flow channel side were examined, respectively. The diagrams reveal that the pressure drop at the three positions for each electrolyte differs significantly, with the flow channel side exhibiting the largest pressure drop, the membrane side the smallest, and the electrode center falling in between. Differences in pressure drops are also observed among the electrolytes; the pressure drop of the  $\text{FeCl}_2$  DES electrolyte is 1.3 times larger than that of TEMPO, and the pressure drop of the  $\text{VCl}_3$  DES electrolyte is 1.2 times larger than that of Quinoxaline. This indicates that the internal pressure drop in the flow battery is influenced by the electrolyte. The differences in pressure drop are mainly due to the differences in the physical and chemical properties of the electrolytes, such as viscosity and conductivity. The viscosity of the electrolyte directly affects the state of laminar or turbulent flow of the fluid, as well as flow resistance in the macroscopic structure. Higher viscosity increases flow resistance, leading to relatively higher pressure drops within the electrodes. Additionally, the conductivity of the electrolyte also impacts the pressure drop to some extent. Higher conductivity means that the migration rate of ions in the electrolyte is higher, which, as charge carriers, helps reduce the mass transfer resistance within the electrolyte, thereby reducing the local resistance in the electrochemical reaction zone and thus lowering the pressure drop during the operation of the flow battery. According to the previous studies, the viscosity of  $\text{FeCl}_2$  and  $\text{VCl}_3$  DES electrolytes is higher than that of TEMPO and Quinoxaline DES electrolytes, while the conductivity of TEMPO and Quinoxaline DES electrolytes is greater; hence, the pressure drops in the porous electrodes are higher for the  $\text{FeCl}_2$  and  $\text{VCl}_3$  DES electrolytes.

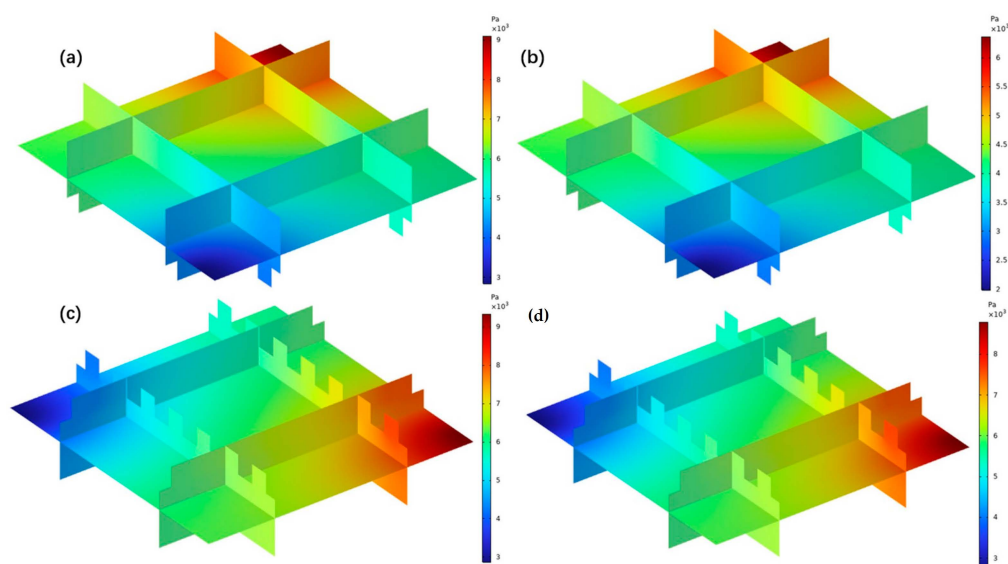


**Figure 8.** Cloud diagram of pressure drop distribution in electrodes with different electrolytes. (a)  $\text{FeCl}_2$ , (b) TEMPO, (c)  $\text{VCl}_3$ , (d) and Quinoxaline.



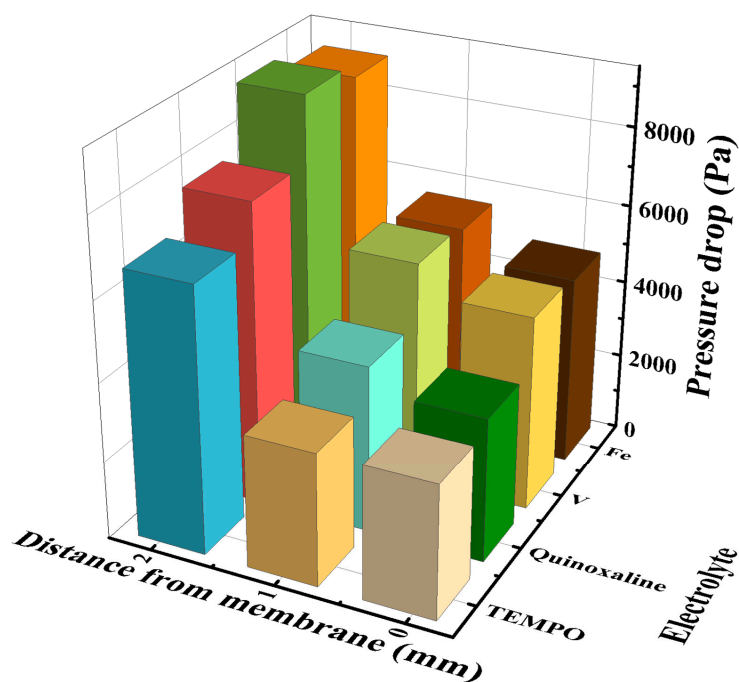


**Figure 9.** Pressure drop at different locations for different electrolytes.

### 3.2. Impact of Different Redox Couples Electrolytes on Electrochemical Performance

In flow batteries, the uniformity of electrolyte concentration within porous electrodes is crucial for the battery's electrochemical performance. A non-uniform concentration distribution leads to inconsistent electrochemical reaction rates, thereby affecting the utilization of the active regions of the electrodes. Additionally, non-uniform concentration not only causes concentration polarization, but also increases the internal resistance of the battery, consequently reducing the battery's energy efficiency and power density. Over prolonged operation, an uneven distribution of electrolyte concentration can accelerate the uneven aging of electrode materials, impacting the battery's stability and lifespan.

To explore this, this study investigated the concentration distributions of the  $\text{FeCl}_2$ , TEMPO,  $\text{VCl}_3$ , and Quinoxaline DES electrolytes within porous electrodes, as shown in the three-dimensional distribution cloud diagrams in Figure 10. Comparing the two positive solutions ( $\text{FeCl}_2$  and TEMPO) and the two negative solutions ( $\text{VCl}_3$  and Quinoxaline), it was found that all the four electrolytes exhibited various degrees of non-uniformity in concentration distribution within the electrodes. However, the TEMPO and Quinoxaline DES electrolytes demonstrated higher uniformity compared to  $\text{FeCl}_2$  and  $\text{VCl}_3$ . This difference reflects the unique mass transfer characteristics of each electrolyte and the complex interactions between the different electrolytes and the electrodes. Due to their lower viscosity and higher conductivity and smaller pressure drops within the electrodes, the TEMPO and Quinoxaline DES electrolytes exhibit better flowability. This results in a more uniform concentration distribution of the electrolyte within the electrodes, reducing the ion concentration differences between the inlet and outlet and alleviating the degree of concentration polarization within the electrodes. Moreover, a uniform concentration distribution helps the electrolyte penetrate better into the internal pores of the electrodes, increasing the utilization rate of the electrode's effective area, thereby enhancing the battery's performance and efficiency.

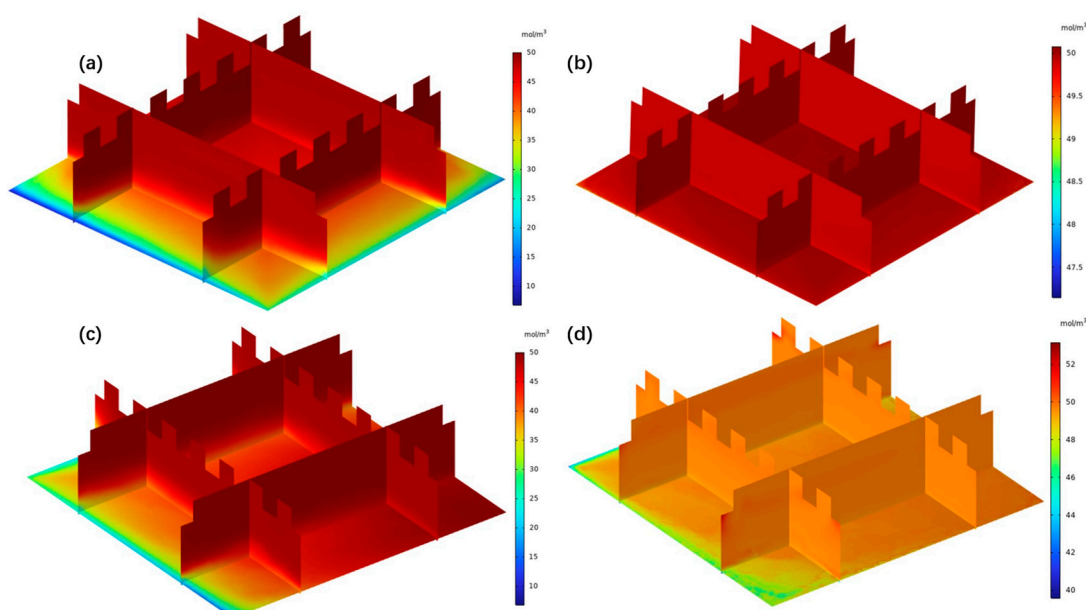


**Figure 10.** Cloud plot of concentration distribution of different electrolytes in electrodes. (a)  $\text{FeCl}_2$ , (b) TEMPO, (c)  $\text{VCl}_3$ , (d) and Quinoxaline.

Overpotential is an additional potential loss that occurs during the charging and discharging processes due to electrochemical reactions and material transfer limitations. In inefficient batteries, the voltage loss caused by overpotentials means that the battery consumes more energy during charging and discharging, reducing the energy conversion efficiency of the battery. Furthermore, overpotentials can also cause an increase in ion concentration gradients within the electrolyte, affecting the effective transfer of ions and increasing the internal resistance of battery, which further reduces the cell performance. To this end, this section explores the distribution of overpotentials within the porous electrodes of the  $\text{FeCl}_2$ , TEMPO,  $\text{VCl}_3$ , and Quinoxaline DES electrolytes.

The three-dimensional overpotential distribution cloud diagrams (Figure 11) visually demonstrate that using the TEMPO and Quinoxaline DES electrolytes can effectively reduce the overpotentials in DES flow batteries, implying lower potential losses during electrochemical redox reactions. Regarding the distribution of overpotentials along the direction of electrolyte flow within the electrodes (as shown in Figure 12), the overpotentials for the positive electrolyte solutions,  $\text{FeCl}_2$  and TEMPO, are approximately 61.5 mV and 35 mV, respectively. However, those for the negative electrolyte solutions,  $\text{VCl}_3$  and Quinoxaline, are about 2.5 mV and 21 mV, respectively. The TEMPO and Quinoxaline DES electrolytes, compared to  $\text{FeCl}_2$  and  $\text{VCl}_3$ , respectively, reduced the overpotentials by 95.9% and 40%. This can be attributed to the more uniform concentration distribution of the TEMPO and Quinoxaline DES electrolytes within the porous electrodes, ensuring that each point on the electrode surface can adequately contact the reactants. This means that electrochemical reactions can occur steadily across the electrode surface rather than being limited to specific areas. When the reactants are unevenly distributed across the electrode surface, certain areas might display slower reaction rates due to a lack of reactants, requiring higher voltages to drive the same chemical reactions, thus increasing the energy losses. Additionally, an uneven concentration distribution can also lead to uneven current densities across the electrode surface, causing some areas to undergo excessive reactions. Excessive reactions can lead to rapid decreases in ion concentration in localized areas, while other areas maintain higher ion concentrations, forming local concentration gradients, thus increasing the concentration overpotentials. Therefore, the uniform concentration distribution of TEMPO and Quinoxaline DES electrolytes effectively reduces activation

overpotentials and concentration overpotentials, presenting lower overpotentials and providing a boost to battery performance.

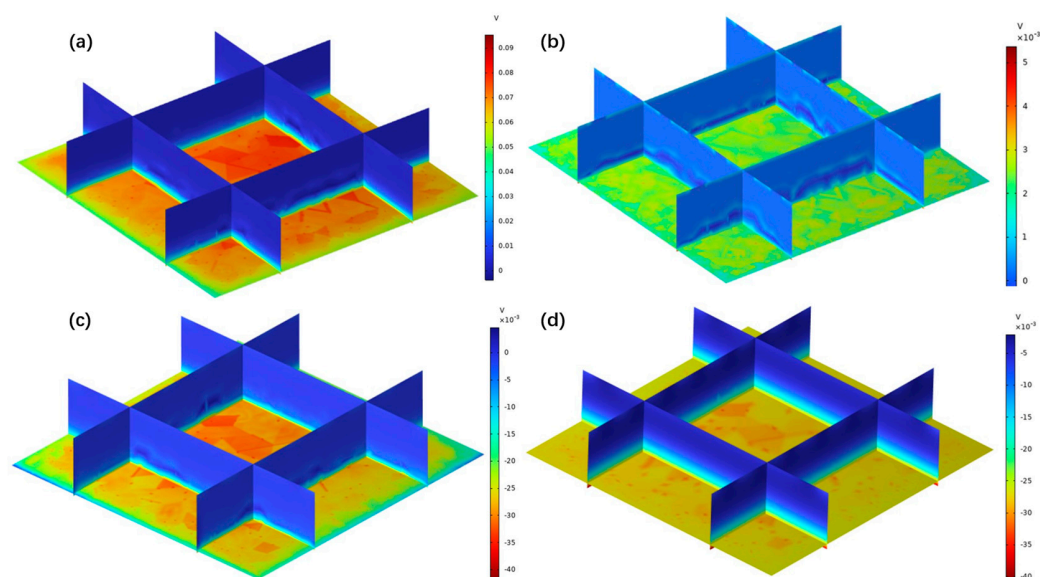


**Figure 11.** Cloud diagram of overpotential distribution of different electrolytes in electrodes. (a)  $\text{FeCl}_2$ , (b) TEMPO, (c)  $\text{VCl}_3$ , (d) and Quinoxaline.

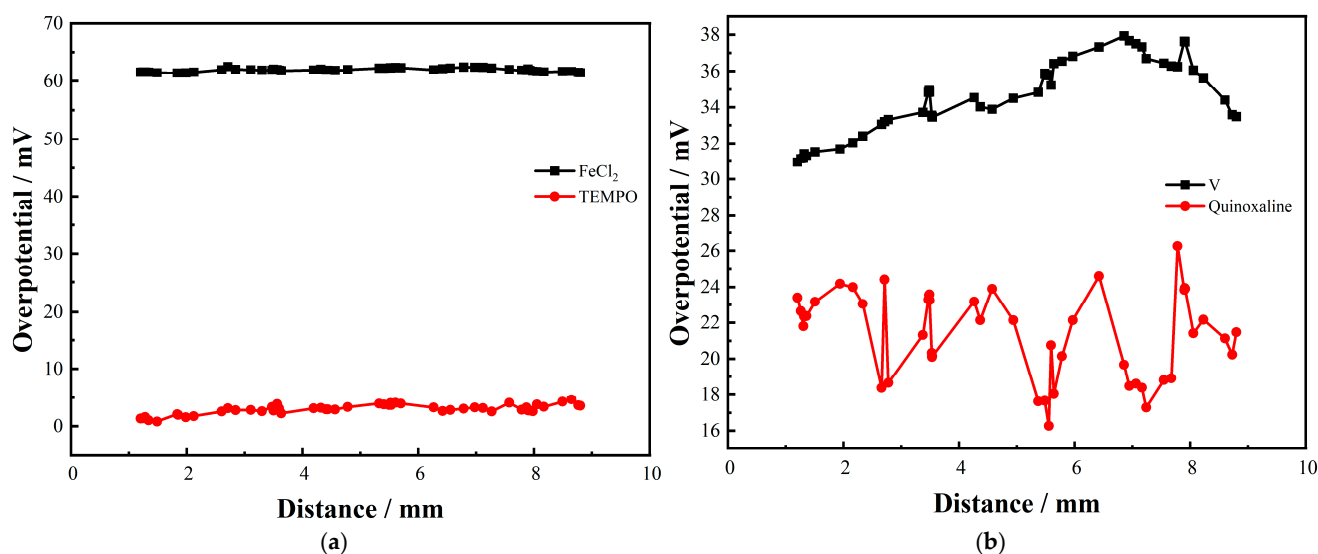


**Figure 12.** Distribution of overpotentials in electrodes along the direction of electrolyte flow. (a) Positive overpotential distribution; (b) negative overpotential distribution.

Figure 13 shows that there are significant differences in the average overpotentials at different distances from the membrane. On the surface of the flow battery electrodes, it is observed that the average overpotential increases significantly closer to the membrane adjacent areas. This phenomenon reveals that electrochemical reactions primarily occur near the membrane, which can be attributed to far superior electronic conductivity in the electrodes compared to effective ionic conductivity in the electrolyte. Therefore, in the DES flow batteries, the limitation of electrochemical reactions primarily stems from the ion transport process but not the electron transport process, indicating that ion migration in the electrolytes is the key factor in optimizing flow battery performance [34]. This conclusion emphasizes that enhancing the ion transport efficiency in the electrolyte is crucial when aiming to improve flow battery performance. Consideration should be given to using

electrolytes with high ionic conductivity, enhancing the material transport characteristics at the membrane–electrode interface. Future research needs to delve deeper into the interactions between ion transport near the membrane and electrochemical reaction kinetics and how these interactions affect the specific mechanisms of flow battery performance to guide the achievement of more efficient energy conversion and a longer battery life.

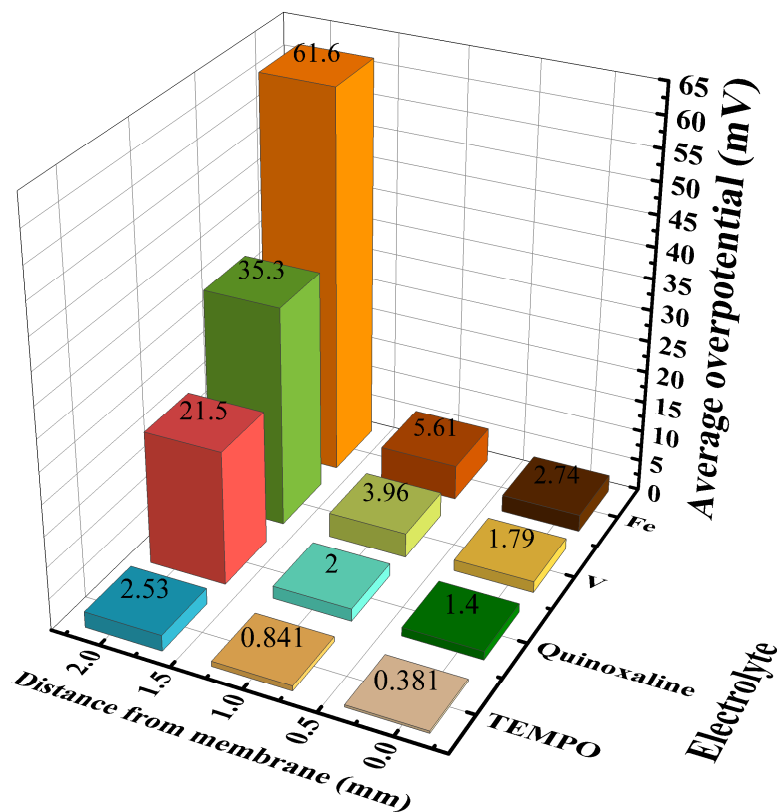


Figure 13. Comparison of average overpotentials of different DES electrolytes at different positions.

#### 4. Conclusions

This research developed a macro-scale, three-dimensional model of a non-aqueous DES electrolyte flow battery. Through the comparison of the simulation data with the experimental observations, the feasibility of the model was validated. This model was used to study the flow characteristics and electrochemical performance of the different redox couple electrolytes in the porous electrodes of the flow batteries. This research found that the flow velocity distribution of the electrolyte has a certain impact on mass transfer efficiency. A uniform flow velocity distribution helps ensure a continuous supply of reactants on the electrode surfaces, thereby enhancing the electrochemical reaction kinetics of the battery.

By comparing the electrolytes of four different redox couples— $\text{FeCl}_2$ , TEMPO,  $\text{VCl}_3$ , and Quinoxaline—it was observed that despite the differences in redox couples, the flow velocity distribution within the electrodes showed similarities due to the consistency of the electrode and the flow channel design. This indicates that in the design of flow batteries, the electrode structure, and the flow channel design have a greater impact on controlling the flow of the electrolyte than the physical and chemical properties of the electrolyte itself. Further investigations into the flow resistance or pressure drops revealed that the  $\text{FeCl}_2$  and  $\text{VCl}_3$  DES electrolytes exhibit larger pressure drops within the electrodes, whereas the TEMPO and Quinoxaline DES electrolytes show smaller pressure drops and better uniformity. This demonstrates that physical and chemical properties such as the

viscosity and conductivity of the electrolytes are the key factors affecting the distribution of pressure drops.

Additionally, it was found that the TEMPO and Quinoxaline DES electrolytes have a more uniform concentration distribution within the electrodes. Such uniform distribution helps reduce the activation overpotentials and concentration polarization, resulting in lower overall overpotentials, which positively impacts battery performance. Finally, this study also explored the differences in average overpotentials near the membrane, finding a significant increase in the average overpotentials closer to the membrane-adjacent areas. This further confirms that the electrochemical reactions in DES electrolyte flow batteries primarily occur near the membrane and are limited by the ion transport process rather than electron transport. These findings emphasize the importance of optimizing the ion transport characteristics of the electrolyte to enhance the electrochemical reactions at the membrane–electrode interface when improving flow battery performance.

In conclusion, the flow characteristics and concentration distribution of the electrolyte significantly impact the performance of flow batteries. Future research should consider optimizing the electrolyte composition and ratio design for electrolytes with different redox couples, aiming to enhance the energy conversion efficiency and extend the lifespan of redox flow batteries.

**Author Contributions:** Conceptualization, Z.X., R.Z. and Q.X.; methodology, M.L., Z.L. and H.S.; validation, Z.X., R.Z. and Q.X.; formal analysis, Z.X., R.Z., H.L. and Q.X.; investigation, M.L., Q.M. and Z.L.; resources, Z.L., H.L. and H.S.; writing—original draft preparation, Z.X.; writing—review and editing, R.Z. and Q.X.; supervision, Q.M. and Q.X.; project administration, H.S. and Q.X.; funding acquisition, H.S. and Q.X. All authors have read and agreed to the published version of the manuscript.

**Funding:** The authors acknowledge financial support from the Natural Science Foundation of Jiangsu Province (BK20231323) and the National Nature Science Foundation of China (No. 52276066).

**Data Availability Statement:** The data of this study are available from the corresponding authors upon available request.

**Conflicts of Interest:** The authors declare that they have no known competing financial interests or personal relationships that could have appeared to influence the work reported in this paper.

## References

1. State Council of China. Energy Development Strategy Action Plan (2014–2020). 2014. Available online: [https://climate-laws.org/document/energy-development-strategy-action-plan-2014-2020\\_275f](https://climate-laws.org/document/energy-development-strategy-action-plan-2014-2020_275f) (accessed on 10 December 2024).
2. National Development and Reform Commission of China. Energy Technology Innovation Plan of Action (2016–2030). 2016. Available online: <https://www.iea.org/policies/6272-china-energy-technology-innovation-action-plan-2016-2030> (accessed on 10 December 2024).
3. Shi, H.; Xu, H.; Gao, W.; Zhang, J.; Chang, M. The impact of energy poverty on agricultural productivity: The case of China. *Energy Policy* **2022**, *167*, 113020. [[CrossRef](#)]
4. Abdul, D.; Wenqi, J.; Tanveer, A. Environmental stewardship: Analyzing the dynamic impact of renewable energy, foreign remittances, and globalization index on China’s CO<sub>2</sub> emissions. *Renew. Energy* **2022**, *201*, 418–425. [[CrossRef](#)]
5. Shrestha, A.; Mustafa, A.A.; Htike, M.M.; You, V.; Kakinaka, M. Evolution of energy mix in emerging countries: Modern renewable energy, traditional renewable energy, and non-renewable energy. *Renew. Energy* **2022**, *199*, 419–432. [[CrossRef](#)]
6. Li, B.; Guo, J.; Dong, H.; Chen, J. Efficiency analysis of redox flow battery applied in power system. *Proc. CSEE* **2009**, *29*, 1–6.
7. Juarez-Robles, D.; Rauhala, T.; Jeevarajan, J. Exploring the Safety Aspects of Redox Flow Batteries. *ECS Meet. Abstr.* **2022**, *2022*, 44. [[CrossRef](#)]
8. Hou, Z.; Chen, X.; Liu, J.; Huang, Z.; Chen, Y.; Zhou, M.; Liu, W.; Zhou, H. Towards a high efficiency and low-cost aqueous redox flow battery: A short review. *J. Power Sources* **2024**, *601*, 234242. [[CrossRef](#)]
9. Huang, Z.; Mu, A. Flow field design and performance analysis of vanadium redox flow battery. *Ionics* **2021**, *27*, 5207–5218. [[CrossRef](#)]

10. Huang, Z.; Yang, C.; Xie, X.; Yang, B.; Liu, Y.; Guo, Z. Attributes and performance analysis of all-vanadium redox flow battery based on a novel flow field design. *Ionics* **2023**, *29*, 2793–2803. [[CrossRef](#)]
11. Liu, B.; Li, Y.; Jia, G.; Zhao, T. Recent Advances in Redox Flow Batteries Employing Metal Coordination Complexes as Redox-Active Species. *Electrochem. Energy Rev.* **2024**, *7*, 7. [[CrossRef](#)]
12. Puleston, T.; Clemente, A.; Costa-Castelló, R.; Serra, M. Modelling and Estimation of Vanadium Redox Flow Batteries: A Review. *Batteries* **2022**, *8*, 121. [[CrossRef](#)]
13. Zhou, H.; Zhang, R.; Ma, Q.; Li, Z.; Su, H.; Lu, P.; Yang, W.; Xu, Q. Modeling and Simulation of Non-Aqueous Redox Flow Batteries: A Mini-Review. *Batteries* **2023**, *9*, 215. [[CrossRef](#)]
14. Lehmann, M.L.; Tyler, L.; Self, E.C.; Yang, G.; Nanda, J.; Saito, T. Membrane design for non-aqueous redox flow batteries: Current status and path forward. *Chem* **2022**, *8*, 1611–1636. [[CrossRef](#)]
15. Li, Z.G.; Fang, X.T.; Cheng, L.; Wei, X.; Zhang, L. Techno-economic analysis of non-aqueous hybrid redox flow batteries. *J. Power Sources* **2022**, *536*, 231493. [[CrossRef](#)]
16. Su, L.; Ferrandon, M.; Kowalski, J.A.; Vaughey, J.T.; Brushett, F.R. Electrolyte development for non-aqueous redox flow batteries using a high-throughput screening platform. *J. Electrochem. Soc.* **2014**, *161*, A1905–A1914. [[CrossRef](#)]
17. Prabhune, A.; Dey, R. Green and sustainable solvents of the future: Deep eutectic solvents. *J. Mol. Liq.* **2023**, *379*, 121676. [[CrossRef](#)]
18. Meenu, M.; Bansal, V.; Rana, S.; Sharma, N.; Kumar, V.; Arora, V.; Garg, M. Deep eutectic solvents (DESs) and natural deep eutectic solvents (NADESs): Designer solvents for green extraction of anthocyanin. *Sustain. Chem. Pharm.* **2023**, *34*, 101168. [[CrossRef](#)]
19. Ren, S.H.; Mu, T.C.; Wu, W.Z. Advances in deep eutectic solvents: New green solvents. *Processes* **2023**, *11*, 1920. [[CrossRef](#)]
20. Smith, B.; Zhang, T.; Jones, A. Deep eutectic solvents as new electrolytes for redox flow batteries. *Energy Environ. Sci.* **2014**, *7*, 3985–3992.
21. Li, Z.; Chen, Y.; Liu, X. Modeling of porous electrode behavior in DES-based flow batteries. *J. Electroanal. Chem.* **2021**, *889*, 115197. [[CrossRef](#)]
22. Zhang, T.; Jones, A.; Smith, B. Physicochemical properties of deep eutectic solvents for electrochemical applications. *Chem. Rev.* **2017**, *117*, 8497–8520.
23. Liu, R.; Wang, S.; Gao, Y. Electrochemical properties of TEMPO and quinoxaline-based DES for flow battery applications. *Electrochem. Commun.* **2019**, *102*, 46–51. [[CrossRef](#)]
24. Chen, J.; Li, Y.; Wang, H. Recent advances in deep eutectic solvents for redox flow batteries. *Electrochim. Acta* **2022**, *426*, 140781. [[CrossRef](#)]
25. Weber, A.Z.; Newman, J. Modeling transport in polymer-electrolyte fuel cells. *Chem. Rev.* **2006**, *106*, 4125–4144.
26. Kreuer, K.D. On the development of proton conducting polymer membranes for hydrogen and methanol fuel cells. *J. Membr. Sci.* **2001**, *185*, 29–39. [[CrossRef](#)]
27. Bird, R.B.; Stewart, W.E.; Lightfoot, E.N. *Transport Phenomena*, 2nd ed.; John Wiley & Sons: New York, NY, USA, 2007.
28. Biesheuvel, P.M.; Bazant, M.Z. Nonlinear dynamics of capacitive charging and desalination by porous electrodes. *Phys. Rev. E* **2010**, *81*, 031502. [[CrossRef](#)]
29. Srinivasan, S.; Weidner, J.W.; Botte, G.G. Steady-state and transient models of electrochemical systems. *Electrochim. Acta* **1999**, *44*, 3699–3709.
30. Chen, H.; Cheng, M.; Feng, X.; Chen, Y.; Chen, F.; Xu, J. Analysis and optimization for multi-stack vanadium flow battery module incorporating electrode permeability. *J. Power Sources* **2021**, *515*, 230606. [[CrossRef](#)]
31. Fraser, E.J.; Ranga Dinesh, K.K.J.; Wills, R.G.A. A two dimensional numerical model of the membrane-divided soluble lead flow battery. *Energy Rep.* **2021**, *7*, 49–55. [[CrossRef](#)]
32. Dickinson, E.J.F.; Wain, A.J. The Butler-Volmer equation in electrochemical theory: Origins, value, and practical application. *J. Electroanal. Chem.* **2020**, *872*, 114145. [[CrossRef](#)]
33. Hall, D.M.; Grenier, J.; Duffy, T.S.; Lvov, S.N. The Energy Storage Density of Redox Flow Battery Chemistries: A Thermodynamic Analysis. *J. Electrochem. Soc.* **2020**, *167*, 110536. [[CrossRef](#)]
34. Zhou, X.L.; Zhao, T.S.; An, L.; Zeng, Y.K.; Yan, X.H. A vanadium redox flow battery model incorporating the effect of ion concentrations on ion mobility. *Appl. Energy* **2015**, *158*, 157–166. [[CrossRef](#)]
35. Xu, J.; Ma, Q.; Xing, L.; Li, H.; Leung, P.; Yang, W.; Su, H.; Xu, Q. Modeling the effect of temperature on performance of an iron-vanadium redox flow battery with deep eutectic solvent (DES) electrolyte. *J. Power Sources* **2020**, *449*, 227491. [[CrossRef](#)]
36. Zhang, R. Performance Study of Redox Flow Battery with Deep Eutectic Solvents (DES) Modified Electrodes and Electrolyte Composed of Organic Active Materials in Deep Eutectic Solvent. Ph.D. Thesis, Jiangsu University, Zhenjiang, China, 2024.
37. Casas, J.M.; Crisóstomo, G.; Cifuentes, L. Speciation of the Fe(II)–Fe(III)–H<sub>2</sub>SO<sub>4</sub>–H<sub>2</sub>O system at 25 and 50 °C. *Hydrometallurgy* **2005**, *80*, 254–264. [[CrossRef](#)]

38. Leung, P.; Aili, D.; Xu, Q.; Rodchanarowan, A.; Shah, A.A. Rechargeable organic–air redox flow batteries. *Sustain. Energy Fuels* **2018**, *2*, 2252–2259. [[CrossRef](#)]
39. Winsberg, J.; Hagemann, T.; Janoschka, T.; Hager, M.D.; Schubert, U.S. Redox-Flow Batteries: From Metals to Organic Redox-Active Materials. *Angew. Chem. Int. Ed.* **2017**, *56*, 686–711. [[CrossRef](#)] [[PubMed](#)]
40. Nicholson, R.S.; Shain, I. Theory of Stationary Electrode Polarography: Single Scan and Cyclic Methods Applied to Reversible, Irreversible, and Kinetic Systems. *Anal. Chem.* **1964**, *36*, 706–723. [[CrossRef](#)]
41. Laviron, E. Adsorption, Autoinhibition and Autocatalysis in Polarography and in Linear Potential Sweep Voltammetry. *J. Electroanal. Chem.* **1979**, *101*, 19–28. [[CrossRef](#)]
42. Zhao, L.; Ma, Q.; Xu, Q.; Su, H.; Zhang, W. Performance improvement of non-aqueous iron-vanadium flow battery using chromium oxide–modified graphite felt electrode. *Ionics* **2021**, *27*, 1–11. [[CrossRef](#)]

**Disclaimer/Publisher’s Note:** The statements, opinions and data contained in all publications are solely those of the individual author(s) and contributor(s) and not of MDPI and/or the editor(s). MDPI and/or the editor(s) disclaim responsibility for any injury to people or property resulting from any ideas, methods, instructions or products referred to in the content.